ADVANCED MATERIALS
www.advmat.de

Backbone Tailoring Enables High-Performance and Stable n-Type Organic Mixed Ionic-Electronic Conductors for Synaptic Simulation and Biosensor

*Wanli Yang, Suxiang Ma, Sergio Gámez-Valenzuela, Sang Young Jeong, Jin-Woo Lee, Haihui Cai, Rongjin Zhu, Bin Liu, Han Young Woo, Bumjoon J. Kim, Shu-Jen Wang, Paddy Kwok Leung Chan, Xugang Guo, and Kui Feng**

High-performance and stable n-type organic mixed ionic-electronic conductors (OMIECs) are crucial for advancing organic electrochemical transistors (OECTs)-based low-power complementary circuits and biosensors, yet their development remains a great challenge. Herein, the study presents a series of donor-acceptor polymers incorporating bithiophene (BTI) and fused BTI derivatives with varying conjugation backbone lengths as acceptors. The mid-size fused BTI dimer enables polymer PBTI2g-DTCN with simultaneously improved ion-uptake capability, film structural order, and ion/electron transport capability. Consequently, an impressive electron mobility of 0.84 $cm^2\ V^{-1}\ s^{-1}$ and a record figure-of-merit (μC^*) of 287.8 $F\ cm^{-1}\ V^{-1}\ s^{-1}$ are achieved for PBTI2g-DTCN-based n-type conventional OECT in accumulation mode, while the vertical OECTs (vOECTs) attain a state-of-the-art area-normalized transconductance ($g_{m,A}$) of 71.8 $\mu S\ \mu m^{-2}$ with remarkable operational stability. Through finely manipulating the channel components, the vOECTs demonstrate dual-mode operation, switching between non-volatile and volatile states. In non-volatile mode, vOECT-based artificial synapses with excellent ambient stability enable dynamic learning and are employed in convolutional neural networks for image recognition. In volatile mode, they excel in biosensing, monitoring electrocardiography and electromyography signals. These remarkable results demonstrate that backbone tailoring is a powerful strategy for developing high-performance n-type OMIECs for synaptic and sensor applications.

1. Introduction

Organic electrochemical transistors (OECTs) form the foundation of numerous emerging organic bioelectronic technologies, spanning from biochemical sensing[1–4] to analogue neuromorphic computing[5–7] as well as low-voltage amplifiers and circuits.[8–11] This versatility stems from their volumetric capacitances and unique coupling of ionic and electronic charge carriers in an organic mixed ionic-electronic conductor (OMIEC).[12] So far, major progress has been achieved for p-type OECTs with a sizable figure-of-merit μC^* (charge transport mobility, μ; volumetric-normalized capacitance, C^*) exceeding 500 $F\ cm^{-1}\ V^{-1}\ s^{-1}$.[2,13–16] However, the development of n-type counterparts lags greatly behind, with the μC^* values typically below 200 $F\ cm^{-1}\ V^{-1}\ s^{-1}$.[17–20] Notable examples of n-type OECT materials include amide-functionalized (hetero)arene-based polymers,[21–25] imide-functionalized (hetero)arene-based polymers,[26–31] and ladder-type polymers.[32–35] Although the C^* values of these n-type polymers are on par with those of p-type counterparts, their mobility values typically range from 0.01 to 0.1 $cm^2\ V^{-1}\ s^{-1}$, significantly lower than those of p-type ones (>1.0 $cm^2\ V^{-1}\ s^{-1}$).[17] This mismatch in performance between p-type and n-type OECTs limits the development of low-power complementary devices, artificial synapses, and biosensors.[36–38] Therefore, it is critical to develop new n-type polymers with improved charge mobility while maintaining

W. Yang, S. Ma, S. Gámez-Valenzuela, H. Cai, R. Zhu, B. Liu, X. Guo, K. Feng
Department of Materials Science and Engineering
Southern University of Science and Technology
Shenzhen, Guangdong 518055, China
E-mail: fengk@sustech.edu.cn
W. Yang, P. K. L. Chan
Department of Mechanical Engineering
The University of Hong Kong
Pokfulam Road, Hong Kong 999077, China
The ORCID identification number(s) for the author(s) of this article can be found under https://doi.org/10.1002/adma.202512070
S. Y. Jeong, H. Y. Woo
Department of Chemistry
Korea University
Anamro 145, Seoul 02841, Republic of Korea
J.-W. Lee, B. J. Kim
Department of Chemical and Biomolecular Engineering
Korea Advanced Institute of Science and Technology
Daejeon 34141, Republic of Korea
S.-J. Wang
Department of Physics
Hong Kong Baptist University
Kowloon Tong, Hong Kong 999077, China

DOI: 10.1002/adma.202512070

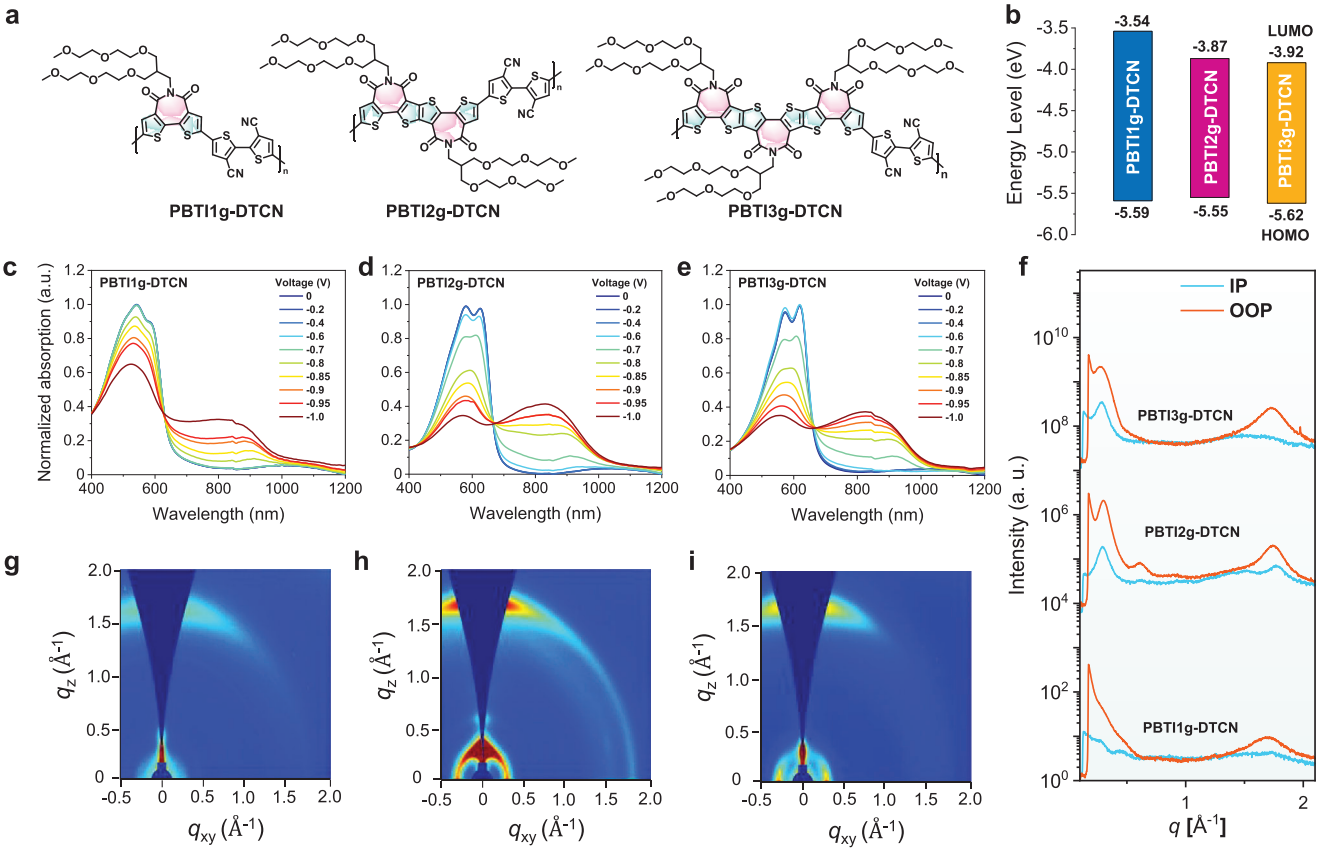

Figure 1. a) Molecular structures of PBTI1g-DTCN, PBTI2g-DTCN, and PBTI3g-DTCN. b) FMO alignment of three polymers. UV–vis–NIR spectroelectrochemical measurements of c) PBTI1g-DTCN, d) PBTI2g-DTCN, and e) PBTI3g-DTCN thin films in 0.1 M NaCl aqueous solution at different reduction voltages against Ag/Ag^+ reference. f) 2D-GIWAXS line-cut profiles along the in-plane and out-of-plane directions. 2D-GIWAXS images of g) PBTI1g-DTCN, h) PBTI2g-DTCN, and i) PBTI3g-DTCN thin films fabricated by spin-coating.

a high ion-uptake/transport capability to advance bioelectronic applications.

Adapting proven approaches in organic thin-film transistors (OTFTs), such as fine-tuning the π-conjugated backbone, developing new building blocks, optimizing side chains, and minimizing device contact resistance,[39–41] is an available strategy for accessing n-type OECT materials with high mobility. Among them, fine-tuning π-conjugated backbone, known for its ability to access high-mobility n-type OTFTs, presents a promising avenue for accessing high-performance n-type OECTs.[42] Ladder-type bithiophene imide (BTI) derivatives (BTIn) with controllable conjugation lengths have demonstrated considerable success in constructing n-type polymers with controllable conjugation backbones, thus achieving impressive OTFT electron mobility ($\mu_{e,\,OTFT}$ >3 $cm^2\ V^{-1}\ s^{-1}$).[43,44] To investigate how conjugated backbone extension influenced the molecular topology and electronic structure in BTIn, we performed density functional theory (DFT) calculations. It was found that the lowest unoccupied molecular orbital (LUMO) energy levels gradually decrease with the π-conjugation extension of the BTI series, and the calculated backbone geometries demonstrated good coplanarity for them (Figure S1, Supporting Information). In the calculated electrostatic (ESP) potential surface diagram, BTI2 and BTI3 display pronounced negative charge densities between neighboring BTI units, indicating increased electron-deficient characters as the backbone extends in BTIn. Non-covalent interaction analysis exhibited small steric hindrance between thiophenes in three blocks (Figure S2, Supporting Information), which contributes to a favorable planar conformation. Therefore, BTI2 and BTI3, characterized by stronger electron deficiency and longer π-conjugated frameworks compared with BTI1, are promising building blocks for constructing high-performance n-type OMIECs.

Given these appealing properties, we design and synthesize three new donor-acceptor (D-A) OMIECs, PBTI1g-DTCN, PBTI2g-DTCN, and PBTI3g-DTCN (**Figure 1a**), based on BTIn installing branched oligo(ethylene glycol)-type polar side chains as electron-deficient blocks and dicyanated bithiophene (DTCN) as the co-unit. We utilized DTCN as a co-unit due to its strong electron-withdrawing character and good coplanarity.[45] Among them, the mid-sized BTI2-based PBTI2g-DTCN simultaneously shows the most desirable properties for n-type OMIECs, including low frontier molecular orbital (FMO) energy levels (LUMO and highest occupied molecular orbital (HOMO) energy levels), good electrochemical dopability, and distinct structural order compared to the other two polymers. As a result, PBTI2g-DTCN delivers a record μC^* of 287.8 F $cm^{-1}\ V^{-1}\ s^{-1}$ in n-type conventional OECTs (cOECTs) with accumulation mode,

and a high area-normalized transconductance ($g_{m,A}$) of 71.8 μS μm^{-2} in vertical OECTs (vOECTs) with excellent operational stability by blending with a photocurable polymer(cinnamate-cellulose polymer, Cin-Cell). Via mass ratio adjustments of the channel components, the vOECT-based artificial synapses are capable of both volatile and non-volatile operations, thus realizing sensing, memory, and processing for energy-efficient bioelectronics.

2. Results and Discussion

2.1. Synthesis of Polymers

The synthesis of dibrominated monomers BTI1g-2Br and BTI2g-2Br was prepared by following previously reported protocols in the literature.[31,46] The synthetic route to brominated monomer BTI3g-2Br is depicted in Scheme S1a (Supporting Information). Compound 1[46] was first reacted with 3-(2-(2-methoxyethoxy)ethoxy)-2-((2-(2-methoxyethoxy)ethoxy) methyl)propan-1-amine to yield BTI3g, which was subsequently brominated using Br_2 in the presence of a catalytic amount of $FeCl_3$ to afford dibrominated monomer BTI3g-2Br. All the dibrominated monomers were confirmed by $^1H/^{13}C$ nuclear magnetic resonance (NMR) spectroscopy and high-resolution mass spectrometry. These monomers were then subjected to polymerization with distannylated co-monomer DTCN-2Sn via a typical Stille coupling to yield PBTI1g-DTCN, PBTI2g-DTCN, and PBTI3g-DTCN (Scheme S1b, Supporting Information). All three polymers showed excellent solubility in chloroform and hexafluoroisopropanol, and their chemical structures were confirmed by ^1H NMR spectroscopy and elemental analysis. Based on standard gel permeation chromatography (GPC) using hexafluoroisopropanol as eluent (Figure S3, Supporting Information), the molecular weight (M_n)/polydispersity ($Đ$) of PBTI1g-DTCN, PBTI2g-DTCN, and PBTI3g-DTCN were estimated to be 89.5 KDa /2.36, 58.7 KDa /2.18, and 57.6 KDa/1.56, respectively. To demonstrate the reproducibility of our polymerization process, we have prepared two additional batches of PBTI2g-DTCN under identical Stille polymerization conditions (Figure S4, Supporting Information). Good consistency is found in their $M_n/Đ$ values across the three batches, which are 58.7 KDa /2.18, 59.6 kDa/1.38, and 52.3 kDa/1.42 (Table S1, Supporting Information), respectively, thus highlighting the reproducibility of our polymerization methodology. For investigating the residual Sn and Pd contamination during the purification process, we performed inductively coupled plasma mass spectrometry measurements. The results show that both Sn and Pd concentrations in all three polymers are below 1 ppm (Pd<0.02 ppm; Sn<0.7 ppm), which are well within the acceptable ranges for electronic device applications (Table S2, Supporting Information). Thermogravimetric analysis (Figure S5, Supporting Information) shows their high decomposition temperatures of >320 °C, and further differential scanning calorimetry scans (Figure S6, Supporting Information) exhibit no visible thermal transitions for these polymers in the temperature range of 50–250 °C, underscoring their adequacy for OECT device applications.

2.2. Optical and Electronic Properties

The optical properties of three polymers were investigated using ultraviolet-visible (UV–vis) absorption spectroscopy. First, we measured the absorption properties of three monomers to elucidate the conjugated backbone length effects among the BTI series. As shown in Figure S7 (Supporting Information), the maximum absorption peaks (λ_{max}^{soln}s) in solution exhibit a gradual bathochromic shift with increasing conjugated lengths. Among the monomers, BTI2g-2Br shows the most pronounced vibronic shoulder and a significant red shift when transitioning from solution to film, indicating stronger self-aggregation behaviour of BTI2. As expected, three resulting polymers exhibit substantially red-shifted absorption relative to their corresponding monomers (Figure S8, Supporting Information). The λ_{max}^{soln} values are 520, 604, and 612 nm for PBTI1g-DTCN, PBTI2g-DTCN, and PBTI3g-DTCN, respectively. The variable-temperature UV–vis absorption showed that the π–π^* absorption peaks of PBTI2g-DTCN and PBTI3g-DTCN were gradually blenched as temperature increases (Figure S9, Supporting Information), demonstrating strong pre-aggregation characters in solution. A notable bathochromic shift of 15–20 nm is observed for three polymers as transitioning from solution to film, attributed to denser molecular packing and increased aggregation in the solid state. Compared to PBTI1g-DTCN, both PBTI2g-DTCN and PBTI3g-DTCN exhibit distinctive vibronic shoulder peaks in both solution and film states, demonstrating that the extended conjugation length in electron-deficient building blocks can enhance molecular packing and aggregation in polymers.

Based on reduction/oxidation onsets of cyclic voltammetry (CV) curves (Figure 1b; Figure S10, Supporting Information), the E_{LUMO}/E_{HOMO} levels are calculated to be −3.54/−5.59 eV for PBTI1g-DTCN, −3.87/−5.55 eV for PBTI2g-DTCN, and −3.92/−5.62 eV for PBTI3g-DTCN (Table S1, Supporting Information). From PBTI1g-DTCN to PBTI3g-DTCN, the E_{LUMO} levels gradually decrease, indicating effective LUMO suppression by extending the backbone of the electron-deficient building blocks. Ultraviolet photoemission spectroscopy (UPS) and inverse photoemission spectroscopy (IPES) measurements were also used to study the FMO energy levels for three polymers (Figure S11, Supporting Information). The obtained HOMO/LUMO levels, by UPS/IPES methods, are −3.38/−5.45 eV, −3.65/−5.43 eV, and −3.70/−5.52 eV for PBTI1g-DTCN, PBTI2g-DTCN, and PBTI3g-DTCN (Table S3, Supporting Information), respectively. These results are in good agreement with those from CV measurements, both showing a gradual decrease in their LUMO levels with an increase in the BTI monomer size of the polymers. DFT calculations show the same energy level trends obtained from CV results (Figures S12 and S13, Supporting Information). Optimized molecular geometries reveal that PBTI2g-DTCN and PBTI3g-DTCN exhibit a higher degree of backbone coplanarity with dihedral angles typically less than 10° between BTI2/BTI3 and the neighbouring DTCN units compared to PBTI1g-DTCN. These encouraging findings of PBTI2g-DTCN and PBTI3g-DTCN are expected to access higher electron mobility in both n-type OTFTs and OECTs.

Ultraviolet-visible-near infrared (UV–vis–NIR) spectroelectrochemistry measurements were employed to explore the electrochemical doping properties of three polymers. As illustrated in

Figure 1c–e and Figure S14 (Supporting Information), increasing the potentials leads to a gradual decrease in absorption at short wavelengths for all three polymers, accompanied by the appearance of a new absorption band in the NIR region, demonstrating the formation of polarons and/or bipolarons. Notably, the neutral absorptions of PBTI2g-DTCN and PBTI2g-DTCN are almost completely bleached at the highest reduction potential of −1 V, indicative of a highly n-doped state with a promoted electron density in the doped film. By contrast, only a limited reduction of absorption intensities in the neutral absorption is observed for the PBTI1g-DTCN film against the high reduction voltage, suggesting a lower electron density in the doped film. This originates not only from the higher-lying LUMOs of PBTI1g-DTCN but also from the reduced ion-uptake capability as evidenced by electrochemical impedance spectroscopy (EIS) measurements. As shown in Figures S15–S17 (Supporting Information), PBTI2g-DTCN and PBTI3g-DTCN films efficiently uptake ions from aqueous electrolyte, exhibiting large C^* values of 325.4 and 368.8 F cm^{-3}, respectively, higher than that of PBTI1g-DTCN film (283.3 F cm^{-3}), because of the increasing density of polar side chains. Besides, water contact angle measurements indicate a stronger hydrophilicity for PBTI2g-DTCN and PBTI3g-DTCN films, with contact angle (θ) values of 68° and 77°, respectively (Figure S18, Supporting Information), compared to 101° for PBTI1g-DTCN. This demonstrates the superior wettability of PBTI2g-DTCN and PBTI3g-DTCN films. The enhanced electrochemical dopability of PBTI2g-DTCN and PBTI3g-DTCN positions them as advantageous candidates for applications in n-type OECTs.

2.3. Charge Transport and Film Morphology Characteristics

The charge transport properties of the polymers were investigated using top-gate/bottom-contact OTFTs with a device architecture of glass/Au/polymer/CYTOP/Al. PBTI2g-DTCN and PBTI3g-DTCN demonstrated unipolar n-type performance with OTFT electron mobilities ($\mu_{e,\ OTFT}$s) of 0.043 and 0.0009 cm^2 V^{-1} s^{-1} (Figures S19 and S20, Supporting Information), respectively. The substantially improved $\mu_{e,\ OTFT}$s of PBTI2g-DTCN can be attributed to its higher degree of coplanarity and well-ordered film morphology (vide infra). Unfortunately, PBTI1g-DTCN exhibits no discernible n-type OTFT characteristics, likely due to the factors of its high-lying LUMO and the limited conjugation of the BTI1 unit. The superior electron mobility of PBTI2g-DTCN renders it more favorable for developing high-performance n-type OECTs.

To investigate molecular packing and film morphology, atomic force microscopy (AFM) and 2D grazing incidence wide-angle X-ray scattering (2D-GIWAXS) characterizations were performed. AFM height images (Figure S21, Supporting Information) show that PBTI2g-DTCN exhibits a root-mean-square (RMS) roughness of 2.43 nm, higher than that of PBTI1g-DTCN (1.45 nm) and PBTI3g-DTCN (1.82 nm). The 2D-GIWAXS characterization further (Figure 1f) revealed the densely packed character of PBTI2g-DTCN than PBTI1g-DTCN and PBTI3g-DTCN. All three polymers adopt a predominant face-on orientation, with a pronounced lamellar stacking peak (100) along the in-plane (IP) direction and a strong π-π stacking peak (010) along the out-of-plane (OOP) direction.[47] While all the polymers exhibit clear lamellar stacking peaks in the OOP direction, particularly PBTI2g-DTCN, which even shows a distinct second-order lamellar reflection, the intensity of their π-π stacking signals in the OOP direction is significantly stronger than that of the lamellar peaks. This trend, together with the observation of very weak π-π stacking in the IP direction, indicates that all three polymers adopt a predominantly face-on orientation in their molecular packing. The calculated lamellar/π–π stacking distances are 22.0/3.72 Å for PBTI1g-DTCN, 21.4/3.61 Å for PBTI2g-DTCN, and 22.2/3.62 Å for PBTI3g-DTCN (Table S5, Supporting Information). The tighter π-π stacking of PBTI2g-DTCN should facilitate intermolecular charge hopping. Using the Scherrer equation,[48] the coherence lengths ($CCL_{z,010}$ and $CCL_{xy,100}$) of PBTI2g-DTCN are calculated to be 98.5 and 168 Å, respectively, significantly larger than those of PBTI1g-DTCN (53.5 and 125 Å) and PBTI3g-DTCN (78.7 and 126 Å), indicating higher crystallinity of PBTI2g-DTCN. This superior crystallinity and stronger intermolecular interactions of PBTI2g-DTCN contribute to its more efficient charge transport in OTFTs and OECTs (vide infra).

2.4. OECT Performance and Device Stability

The electrochemical performance of three polymers was first characterized using cOECT in a planar structure (**Figure 2a**). Figure 2b and Figure S22 (Supporting Information) illustrate that the three polymers exhibit typical n-type accumulation behaviors upon biasing positive potentials with minimal hysteresis in both transfer and output curves. The average threshold voltage (V_{th}) values are 0.83, 0.77, and 0.72 V for PBTI1g-DTCN, PBTI2g-DTCN, and PBTI3g-DTCN (**Table 1**), respectively, corresponding to the progressively lowered LUMO levels. The highest geometry normalized transconductance ($g_{m,norm}$) and $\mu C^*$for PBTI1g-DTCN-based devices are calculated to be 1.51 S cm^{-1} and 9.81 F cm^{-1} V^{-1} s^{-1}, respectively. To our delight, PBTI2g-DTCN exhibits a significantly enhanced μC^* of 287.8 F cm^{-1} V^{-1} s^{-1}, which is the record value of n-type polymers for accumulation OECTs and far exceeds those of the state-of-the-art n-type polymers (Figure 2c; Table S4, Supporting Information). In contrast, a lower μC^* of 59.2 F cm^{-1} V^{-1} s^{-1} was obtained for the PBTI3g-DTCN-based OECTs. By slightly adjusting the monomer stoichiometry in the Stille coupling reaction, three additional batches of PBTI2g-DTCN were obtained with the Mn/$Đ$ values of 26.3 kDa/1.31 (PBTI2g-DTCN-1), 33.5 kDa/1.37 (PBTI2g-DTCN-2), and 50.2 kDa/1.66 (PBTI2g-DTCN-3) as shown in Figure S23 (Supporting Information). When evaluated in cOECTs, we observed a slight increase in their average μC^* from 223.1 to 236.6 and 252.4 F cm^{-1} V^{-1} s^{-1} when the molecular weight increases (Table S6, Figures S24 and S25, Supporting Information). The highest performance in PBTI2g-DTCN-3 is a synergetic effect of high volumetric capacitance and charge mobility. More importantly, the μC^* performance of all three PBTI2g-DTCN polymers is still much higher than PBTI1g-DTCN/ PBTI3g-DTCN, regardless of their molecular weights. Thus, the chemical structure of the polymers is indeed the dominant factor governing their performance, whereas the molecular weight merely serves as a contributing factor to fine-tune it.

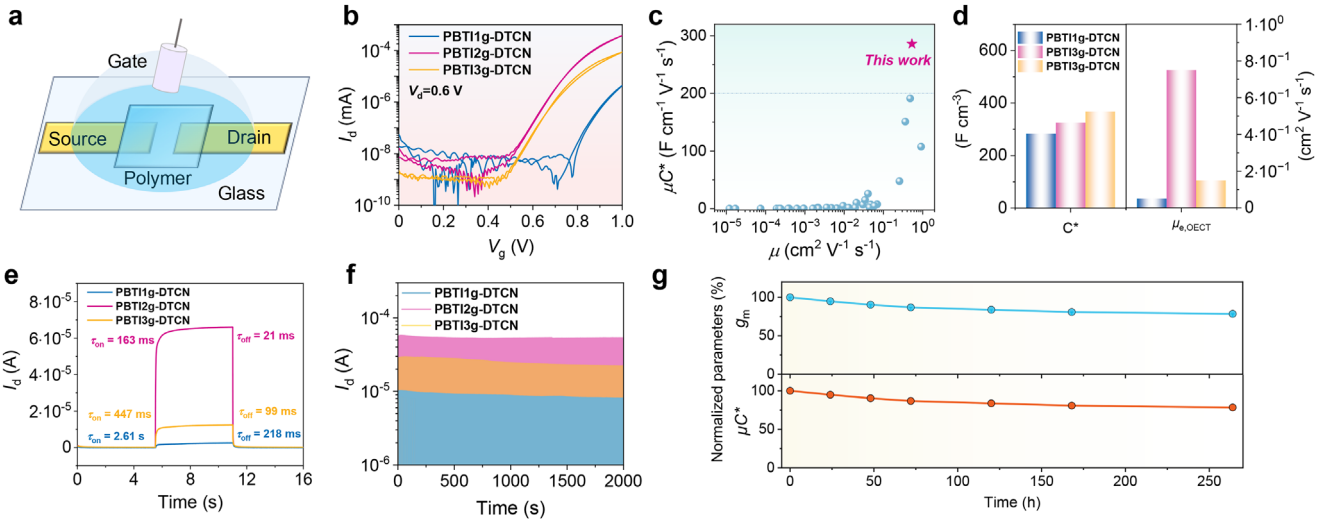

Figure 2. a) Schematic illustration of the cOECT device structure. b) Transfer curves of cOECTs of three polymers. c) A comparison between the μC^* and $\mu_{e,\,OECT}$ values of PBTI2g-DTCN and the representative n-type polymers reported in the accumulation OECTs. d) The C^* and $\mu_{e,\,OECT}$ regimes of three polymers. e) On- and off- time constant of cOECTs based on three polymers. f) Operational stability under sequential square wave gate voltage (V_g = 0.8 V, V_d = 0.6 V). g) Evolution of g_m and μC^* of the optimized PBTI2g-DTCN-based cOECTs in the ambient environment for over 250 h storage.

Based on C^* measurements obtained from EIS, the maximum $\mu_{e,\,OECT}$s are calculated to be 0.04, 0.84, and 0.19 cm^2 V^{-1} s^{-1} for PBTI1g-DTCN, PBTI2g-DTCN, and PBTI3g-DTCN, respectively. PBTI2g-DTCN demonstrates over 5 times higher $\mu_{e,\,OECT}$ than BTI1- and BTI3-based analogues (Figure 2d). Notably, these $\mu_{e,OECT}$ values obtained from OECTs are much higher than $\mu_{e,\,OTFT}$ values extracted from OTFTs in OMIECs. This difference arises from the high polarity of the ethylene glycol side chains, which could induce charge transport traps at the semiconductor/dielectric interface[49] and greatly hinder the charge transport in OTFTs. However, the OECT device operates through a rather different bulk transport mechanism, also at a much higher charge carrier density than OTFTs.[2] As a result, charge transport traps are effectively filled under OECT operating conditions, enabling OECTs to deliver higher device currents and thus higher charge transport mobility than OTFTs.

This outstanding mobility of PBTI2g-DTCN is attributed to its highly ordered polymer chain packing and superior electrochemical doping capability, as confirmed by GIWAXS and UV–vis–NIR spectroelectrochemical results. Following the exponential fitting of the drain current (I_d) versus the switching time, the estimated time constants for the on/off states, denoted as τ_{on}/τ_{off}, were determined to be 2610/218 ms, 163/21 ms, and 447/99 ms for the PBTI1g-DTCN-, PBTI2g-DTCN-, and PBTI3g-DTCN-based devices, respectively (Figure 2e). These values suggest that PBTI2g-DTCN exhibits the most rapid doping/dedoping kinetics. Long-term operational stability of the cOECTs was carried out under pulse mode of gate voltage. All three cOECTs exhibit good stability with the current (I_d) maintaining ≈80% for PBTI1g-DTCN, 93% for PBTI2g-DTCN, and 76% for PBTI3g-DTCN after a total test period of 2000 s (Figure 2f; Figure S26, Supporting Information). Moreover, the PBTI2g-DTCN device can retain ≈78.7% of its initial μC^* value even after 10 days of storage in the ambient environment (Figure 2g).

Compared to cOECTs, vertical OECTs (vOECTs) show distinct advantages through their vertical architecture and specialized electrode design, including an ultra-short channel length and an impermeable top contact (**Figure 3**a; Figure S27, Supporting Information).[1,37,50] This design prevents direct electrolyte contact, making it highly suitable for flexible and implantable monitors that require high transconductance and long-term operational stability. To fabricate vOECTs, we used the high-performing PBTI2g-DTCN blended with a redox-inert photocurable polymer (Cin-Cell, Figure S28, Supporting Information) in an 8:3 mass ratio as an ion-permeable channel. In vOECTs, a high area-normalized transconductance ($g_{m,A}$) of n-type PBTI2g-

Table 1. cOECT performance parameters of three polymers reported in this study.

Polymer	$g_{m,norm}$ [a] [S cm^{-1}]	d [b] [nm]	V_{th} [c] [V]	C^* [F cm^{-3}]	$\mu_{e,OECT}$ [d] [cm^2 V^{-1} s^{-1}]	μC^* [e] [F cm^{-1} V^{-1} s^{-1}]	$I_{on/off}$
PBTI1g-DTCN	1.51(1.47 ± 0.04)	48 ± 2	0.83 ± 0.02	283.3	0.04(0.03 ± 0.004)	9.81(8.60 ± 1.20)	10^3
PBTI2g-DTCN	60.2(58.9± 5.25)	45 ± 2	0.76 ± 0.03	325.4	0.84(0.75 ± 0.10)	287.8(274.1 ± 14.2)	10^5
PBTI3g-DTCN	16.9(15.5 ± 2.91)	41 ± 1	0.72 ± 0.03	368.8	0.19(0.15 ± 0.037)	59.2(56.0 ± 13.6)	10^5

[a] Their maximum values with the average values and the standard deviation given in parentheses. Five samples were tested for each OMIEC. [b] Average thickness calculated by profilometer. [c] Extracted from the x-intercept of the $I_d^{0.5}$-V_g linear fitting. [d] Calculated from OECT-measured μC^* and EIS-measured C^* value. [e] Extracted using saturation regime equation: $g_m = \frac{Wd}{L} \times \mu C^* \times (V_g - V_{th})$, where g_m, W, L, d, V_g, and V_{th} are the peak transconductance, channel width, channel length, film thickness, the applied gate voltage, and threshold voltage, respectively. W = 100 µm, L = 10 µm.

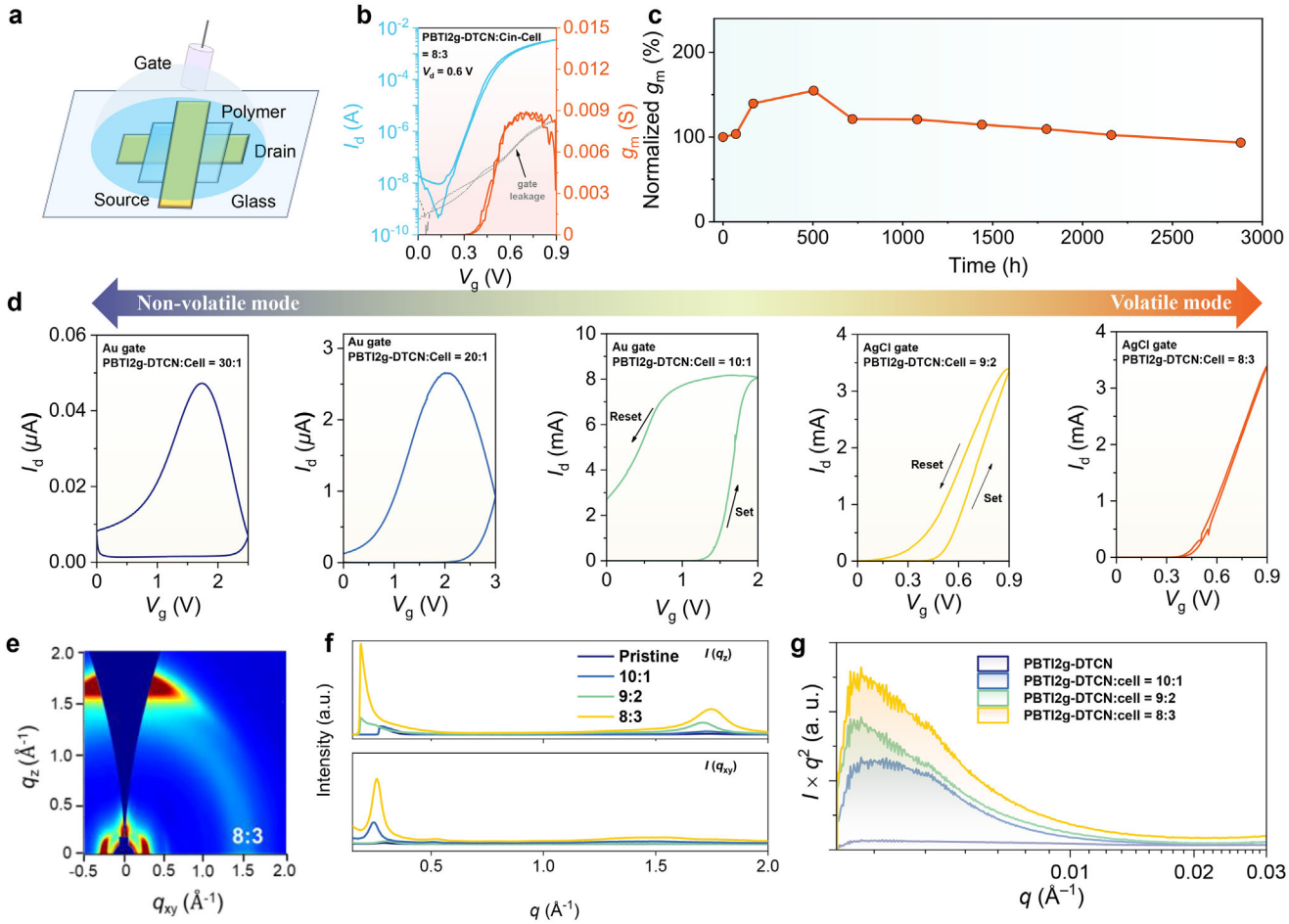

Figure 3. a) Schematic illustration of vOECT device structure. b) Transfer and transconductance characteristics of vOECTs based on PBTI2g-DTCN blended with Cin-Cell. c) Evolution of g_m the optimized vOECTs in the ambient environment for over 2800 h storage. d) Transfer curves of PBTI2g-DTCN-based vOECTs operating in dual mode with different PBTI2g-DTCN: Cin-Cell blending ratios. e) 2D-GIWAXS patterns of PBTI2g-DTCN: Cin-Cell blends in the film state with the mass ratio of 8:3 and f) the corresponding line-cut profiles of pristine and blending films prepared by drop-casting in different mass ratios along the out-of-plane and in-plane directions. g) RSoXS characterization of the pristine and blending films in different mass ratios.

DTCN was calculated to be 71.8 μS μm^{-2}. The leakage current is negligible (< 0.1% channel current) under normal operation (Figure 3b; **Table 2**). Additionally, its p-type counterpart g4T2-T2 in a 6:4 blending ratio with Cin-Cell was used for complementary circuits, achieving an average $g_{m,A}$ of 24.8 μS μm^{-2}. The n- and p-type OMIECs exhibit comparable C^* (Figure S29, Supporting Information), with the absolute sum of their V_{th}s being ≈0.25 V. This feature suggests their suitability for constructing vertical logic circuits with both high performance and low power usage. More importantly, the vOECT based on PBTI2g-DTCN exhibited excellent stability, with g_m maintaining 93.4% of its initial values even after 2800 h of air storage (Figure 3c), underscoring its strong potential for long-term applications. The exceptional operational stability of the vOECTs is attributed to both the device encapsulation strategy and the polymer morphology. On the one hand, the vertical OECT configuration can inherently enhance device stability: the top electrode serves as a rigid protective cap that suppresses film delamination and minimizes interfacial degradation during ion injection/extraction.[1] On the other hand, the blended polymer: Cin-Cell active layer contributes to additional structural robustness. The blend suppresses polymer dissolution and morphological relaxation, thereby maintaining

Table 2. Summary of the vOECT performance for PBTI2g-DTCN and g4T2-T2 in volatile mode.

Polymer	d [nm]	V_d [V]	V_{th} [V]	C^* [F cm^{-3}]	g_m [a)] [mS]	$g_{m,A}$ [b)] [μS μm^{-2}]	$I_{on/off}$
PBTI2g-DTCN	209 ± 0.008	0.6	0.50 ± 0.008	506.9	64.6(64.2 ± 3.7)	71.8(71.3 ± 4.11)	10^5
g4T2-T2	364 ± 0.012	−0.4	−0.25 ± 0.003	178.3	2.25(2.15 ± 1.5)	25.0(24.8 ± 1.66)	10^4

[a)] Their maximum values with the average values and standard deviation given in parentheses. Five samples were tested for each OMIEC. [b)] g_m is normalized by the electrochemically active area A ($W \times L$, $W = L = 30$ μm). For vOECT, the channel area is $W \times d$.

the integrity of the conduction pathways even after extended exposure to air.

Through material and device characterizations, we established structure-property correlations for this series of polymers. Among the three polymers, PBTI2g-DTCN displays relatively low LUMO levels, high volumetric capacitance, and more importantly, good electron mobility, which all contribute to its excellent μC^* performance. Specifically, the low LUMO level of PBTI2g-DTCN over PBTI1g-DTCN comes from its extended polymer backbone conjugation length, enabled by the enhanced delocalization in longer BTI2 monomer over BTI1 monomer. The high volumetric capacitance of PBTI2g-DTCN not only comes from its high side chain density and good hydrophilicity for efficient ion uptake process, but also comes from its good dopability as a result of low LUMO level. The key advantage of PBTI2g-DTCN over PBTI3g-DTCN/PBTI1g-DTCN is its high electron mobility, which comes from its superior structural order compared to the other two polymers. Higher crystallinity in PBTI2g-DTCN film is revealed by GIWAXS measurement, in both π-stacking and lamellar-stacking directions, than in PBTI3g-DTCN/PBTI1g-DTCN films. This would greatly facilitate the inter-chain charge transport process in PBTI2g-DTCN, while the intra-chain charge transport process is benefited by its rigid planar backbone structure, all contributing to the remarkable electron mobility of PBTI2g-DTCN.

2.5. Design Strategies for Dual-Mode OECTs

While the incorporation of Cin-Cell in vOECTs has significantly enhanced the ionic doping and dedoping process, it is often overlooked that adjusting the amount of Cin-Cell can also fine-tune the device's operation mode.[37] Many n-type polymers reported to date exhibit volatile characteristics,[21,31,51,52] but there is still a shortage of materials suitable for non-volatile operation. This limitation stems from the complexity of transitioning between volatile and non-volatile states, which requires sophisticated processing techniques to prevent counterions from neutralizing trapped ions in the channel immediately after the removal of reduction voltage (for n-type channel materials), all while maintaining C^* and ion mobility.[21]

To achieve dual operation modes, we prepared a device architecture featuring a deep channel to homogenize the electric field and optimize the depth-to-length ratio ($W/d > 150$). This approach mitigates C^* and ion mobility losses, thereby enhancing multi-modal sensitivity. By fine-tuning the mass ratio of Cin-Cell, we can regulate the crystallization dynamics, enabling a smooth shift between non-volatile and volatile states (Figure 3d; Figures S30–S32, Supporting Information). According to the 2D-GIWAXS characterization (Figure 3e,f; Figure S33 and Table S7, Supporting Information), increasing the mass ratio of Cin-Cell leads to larger $CCL_{z,010}$ values, indicating a more homogeneous phase within the blended film, as confirmed by resonant soft X-ray scattering (RSoXS) analysis (Figure 3g). The crystalline regions of the PBTI2g-DTCN provide robust charge transport pathways, while the Cin-Cell additive creates amorphous zones that buffer volumetric swelling and trap ions, preventing structural fatigue and maintaining consistent ion-electron coupling over time. This phase-separated microstructure not only supports efficient ion-electron coupling but also resists degradation in ambient conditions. As the mass ratio of PBTI2g-DTCN: Cin-Cell blend increases from 30:1 to 20:1, to 9:2, and finally, to 8:3, the microstructure of the blending material gradually stabilizes, expanding lateral charge injection and accelerating charge/discharge processes. The escalating RMS roughness of the films, transitioning from a blend ratio of 10:1 to 8:3, as observed in the height images, may explain the improved effectiveness of lateral doping (Figure S34, Supporting Information). For efficient non-volatile functioning, a channel material microstructure that reduces ionic compensation is essential. A 10:1 blending ratio yields the optimal microstructure for this purpose. Furthermore, the selection of gate electrode types—whether polarized or non-polarized—significantly impacts the processing that prevents counterions compensation. Ag/AgCl, as a non-polarizable electrode, facilitates faradic current through reactions with ions in the electrolyte. This process minimizes voltage drops at the electrode-electrolyte interface (Figure S35, Supporting Information). In contrast, a polarizable Au electrode prevents faradic current and creates larger voltage drops when biased. Therefore, we chose a polarizable Au gate to inhibit counterion compensation during the ionic dedoping process, ensuring effective non-volatile operation.

2.6. Synaptic Plasticity Tuning of Non-Volatility

The n-type PBTI2g-DTCN demonstrates excellent potential as a channel material for organic electrochemical neuronal synapses (OENS) owing to its non-volatile characteristic, which is enhanced by blending with Cin-Cell at a low mass ratio (PBTI2g-DTCN: Cin-Cell = 10:1). By mimicking neuronal synapse signals both in vivo and in vitro, the V_g with square waves of varying frequency, amplitude, and direct current (DC) offset is modulated using a semiconductor analyzer 4200. Short-term voltage-dependent plasticity (SVDP) is observed in an artificial synapse (**Figure 4a**), where single pulses between 1.2 and 2.3 V elicited different responses. With presynaptic voltage (V_{pre}) over 1.5 V, non-volatile behavior of the artificial synapses emerges with spikes lasting over 5 s. In contrast, at V_{pre} = 1.2 V, signals dissipate in just 0.3 s. By adjusting the pulse duration while maintaining constant amplitude, we observe spike-timing-dependent plasticity (STDP). As depicted in Figure 4b, an excitatory postsynaptic current (EPSC) induced by a 1.5 s pulse failed to return to its initial value for over 10 s, whereas shorter pulse durations led to quicker signal dissipation. This behavior, which signifies the transition from short-term plasticity (STP) to long-term plasticity (LTP), highlights the importance of stimulation that is both sufficiently strong and of adequate duration for the formation of robust memories in the human brain. Next, we assess the retention capacity of the OENS with a grounded gate, which is vital for large-scale neural networks. The conductance of OENS is switched between five distinct analog states, with a dynamic range exceeding 1000 (Figure S36, Supporting Information). Remarkably, each state remains stable for over 600 s in ambient air. This performance is comparable to that of state-of-the-art heterostructures using phase-change random-access memory.[53]

Shorter pulse intervals hinder effective ionic relaxation. Sequentially, we investigated pulse modulation at distinct

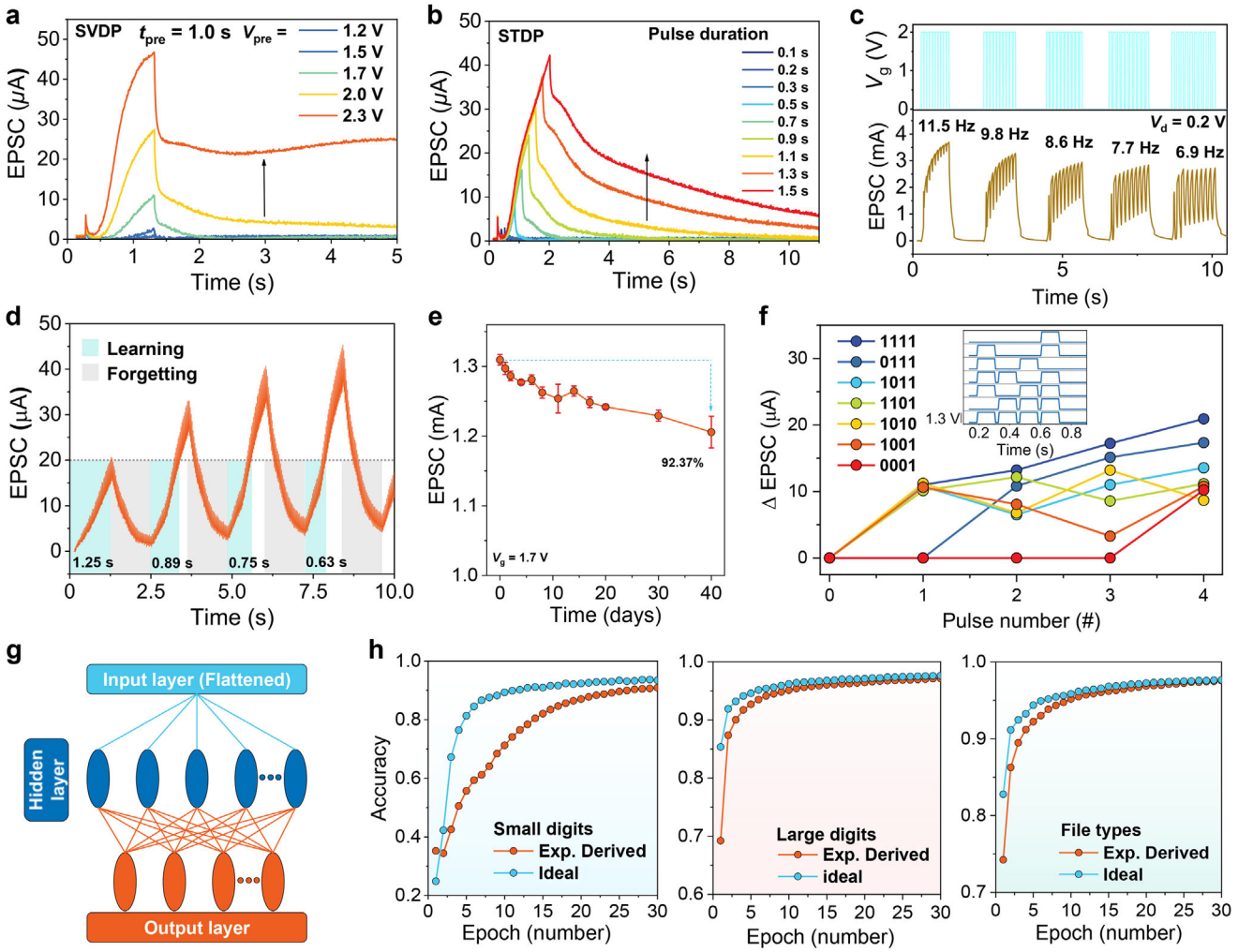

Figure 4. a) SVDP of PBTI2g-DTCN-based OENS with different V_{pre} ranging from 1.2 to 2.3 V, V_d = 0.2 V, t_{pre} = 1.0 s. b) STDP of PBTI2g-DTCN-based OENS with different t_{pre} ranging from 0.1 to 1.5 s, V_d = 0.2 V, V_{pre} = 2.0 V. c) Dynamic filtering characteristics and d) learning behavior simulation based on OENS. e) EPSC responses of PBTI2g-DTCN-based OENS under a single pulse in the ambient environment for over 40 days. f) Separability of PBTI2g-DTCN-based OENS. Seven 4-bit binary digits are illustrated, along with the corresponding square pulse trains that are defined within four timeframes. g) Schematic processing of CNN for simulating the classification accuracy of handwritten digit MNIST dataset. h) The outcomes of backpropagation training for image datasets comprising 8×8 pixel images (small digits), 28×28 pixel images (large digits), and Sandia file classification datasets predicated on experimental data from LTDP.

frequencies to attain dynamic filtering for efficient signal processing (Figure 4c). By applying a sequence of ten consecutive pulses (V_{pre} = 2 V, t_{pre} = 0.08 s) with adjustable intervals (Δt_{pre}), the EPSC magnitude exhibited a frequency-dependent increase as the pulse frequency was raised from 6.9 to 11.5 Hz, indicating that the OENS can work as a dynamic filter similar to biological synapses.[54,55] Further, we examined paired-pulse facilitation (PPF) by applying two consecutive pulses (2.5 V, t_{pre} = 0.1 s) at varying Δt_{pre}, ranging from 0.005 s to 3.0 s (Figure S37, Supporting Information). The PPF index, defined as the ratio of the first accumulated EPSC (A_1) to the pristine one (A_0) (Figure S38, Supporting Information), is a benchmark used to assess synaptic gain and plasticity. PBTI2g-DTCN-based OENS shows superior tunability to paired pulses than earlier research,[54,56] reaching the highest PPF index of 240% at Δt_{pre} = 0.005 s and progressively decreasing to 105% with increasing Δt_{pre}. This PPF response curve fits the formula: PPF index = K_1*exp($-\Delta t/\tau_1$) + K_2*exp($\Delta t/\tau_2$) + Y_0, where Y_0 represents the PPF ratio converging to 100%, K_1 and K_2 are the weights of the paired-pulse facilitation process, and τ_1 and τ_2 are the characteristic relaxation times of the ion in the bulk and channel layer. For PBTI2g-DTCN-based OENS, τ_1 and τ_2 were calculated to be 0.013 and 0.14 s, respectively, aligning well with the behavior of biological synapses. To simulate the learning process in neural networks, we investigated long-term depression and potentiation (LTDP) within the OENS by applying 40 potentiation stimuli (V_{pre} = 2 V, t_{pre} = 0.024 s, Δt_{pre} = 0.006 s) and 40 depression stimuli (V_{pre} = −0.5 V, t_{pre} = 0.024 s, Δt_{pre} = 0.006 s), constituting a single cycle of learning and forgetting (Figure 4d). The channel current increased progressively with each pulse, reaching an EPSC of ≈20 μA during the first learning phase of 1.25 s. In the 4th learning cycle, the EPSC reached the same level in just 0.63 s, illustrating the impact

of repetitive learning on memory retention. The OENS demonstrated 40 distinct multilevel conductance states. The nonlinearity (*NL*) parameters were extracted as $NL_P = 0.61$ for LTP and $NL_D = 1.38$ for LTD, and the symmetry value was calculated to be 12.4 (Figure S39, Supporting Information). The device exhibits relatively symmetric LTP/LTD behavior, demonstrating its suitability for applications demanding precise and balanced synaptic emulation.

To assess real-world practicality, we also evaluated the long-term stability of PBTI2g-DTCN-based synapses without encapsulation under ambient conditions. After storage for 40 days (Figure 4e), the device maintained good stability with the voltage spike retaining 92.37% of its initial amplitude. Furthermore, we evaluated the system's capability to handle binary arithmetic operations by applying seven distinct pulse sequences (1111, 0111, 1011, 1101, 1010, 1001, 0001) and recorded the corresponding output signals (Figure 4f). The analysis reveals that the delayed pulse timing and the increased number of high-level pulses "1" generate stronger output signals, unveiling the system's potential for logical signal differentiation and neuromorphic computing.

Convolutional neural networks (CNNs), as a significant branch of deep learning, provide powerful tools for image recognition and processing.[57,58] Based on the experimental data of LTDP, we developed a three-layer network (Figure 4g; Figure S40, Supporting Information) to conduct backpropagation training on various image datasets. We evaluated the analog performance of the CNN across the Sandia file classification datasets from the MNIST database. Figure 4h demonstrates that after 30 training epochs, the PBTI2g-DTCN-based device achieved high accuracy rates close to the theoretical optimum, specifically 90.9% for small digits, 97.2% for large digits, and 97.6% for file types. The model's exceptional recognition accuracy suggests its capacity to identify minute feature variations, robustness against noise and outliers, and potential as a candidate in versatile neuromorphic computing systems.

2.7. Biosensor in Volatile Mode

Owing to the high transconductance and enhanced stability of the PBTI2g-DTCN: Cin-Cell-based vOECTs with a mass ratio of 8:3 in volatile operation, the capability for in situ and real-time bio-signal detection of PBTI2g-DTCN is assessed through the assembly of complementary inverters (**Figure 5a**; Figure S41, Supporting Information) with its p-type counterpart g4T2-T2 which is also mixed with Cin-Cell in a mass ratio of 6:4. The highest gain value of 188 V V^{-1} was achieved under a supply voltage (V_{dd}) of 0.8 V with the input voltage (V_{in}) sweeping from 0.6 to 1.15 V of a single vertical inverter (Figure 5b), while the highest gain value for conventional inverter was 70 V V^{-1} under a V_{dd} of 1.2 V (Figure S42a, Supporting Information). For the operational stability of vertical inverters, continuous square wave signals (high level: 0.7 V; low level: 0.5 V) were applied as V_{in}, simulating fluctuation of signals within the amplified region. After 2000 s, the inverter retained 92% of its initial output voltage (V_{out}) (Figure 5c). The vertical inverter architecture demonstrates signal amplification capabilities within the 1–20 Hz frequency range (Figure S43, Supporting Information). This limited operational bandwidth stems from intrinsically slow redox processes, including ion diffusion and bulk electrochemical charging of the polymer, which dominate the OECT's RC time constant and thus set the ultimate speed limit for these bioelectronic devices. Next, the inverter was used to amplify the electrocardiogram (ECG) signals. To record the signals, two adhesive medical electrodes were placed on the lower region of the left chest and the upper region of the right chest to provide V_{in} with an external power supply biased to the inverter's maximum gain point. The principal and distinct P-QRS-T waveforms in ECG were detected by vertical inverters (Figure 5f), exhibiting a maximum peak-to-peak amplitude of ≈40 mV, nearly 20 times greater than the signals recorded by inverters utilizing cOECTs (Figure S42b, Supporting Information).

Additionally, a flexible probe was developed to detect electromyogram (EMG) signals (Figure 5d,e). The cOECT and vOECT detectors were fabricated on the polyethylene terephthalate substrate using thermal evaporation and encapsulated by a polydimethylsiloxane layer with an opening for detection. vOECT detectors demonstrated enhanced clarity in resolving muscle tension signals, whereas cOECT-based EMG recordings exhibited significant signal attenuation (Figure 5f; Figure S42b, Supporting Information). This disparity also highlights the superior signal fidelity of vOECT technology in dynamic biomechanical monitoring applications. Moreover, an array of 81 inverters was monolithically organized in a 9 × 9 grid on flexible substrates featuring a vertical traverse structure (Figure 5g,h). Randomly selected performance metrics from inverters across the arrays exhibit notable uniformity, averaging a $g_{m,A}$ of 71.74 μS μm^{-2} for the n-type OECT part, and a gain value of 143.2 V V^{-1} for inverters (Figure 5i; Figure S44, Supporting Information).[59] The deviations in these metrics are all under 10%, attributed to the uniform phase distribution within the blended films. Based on high gain and excellent uniformity, the common gate of the inverter arrays was attached to the underside of leaves, using a typical grounded platinum rod inserted into the soil (Figure 5j). This setup was employed to monitor cellular respiration activities in the absence of light, including phenomena like depolarization, action potentials, and hyperpolarization as depicted in Figure S45 (Supporting Information). Additionally, it captured the current response to illumination switching, as illustrated in Figure 5k. The energy consumption of this system was remarkably low, at less than 3×10^{-7} W, approximately two orders of magnitude lower than current OECT detectors.[60]

In pursuit of advancing the integration of complementary circuits utilizing PBTI2g-DTCN and g4T2-T2-based vOECTs, a suite of logical circuits encompassing NAND, NOR, rectifier, and five-stage ring oscillator was engineered in volatile operation. The associated optical imagery and electrical measurements are presented in Figure S46 (Supporting Information). Both NAND and NOR logic gates function within a voltage range of 0 to 0.8 V, delineating the transition between logic states "0" and "1". For the NAND gate, the output is logic "0" if and only if all inputs ($V_{in\text{-}A}$ and $V_{in\text{-}B}$) are logic "1". In all other cases, the output is logic "1". Conversely, the NOR gate outputs a logic "1" when all inputs ($V_{in\text{-}A}$ and $V_{in\text{-}B}$) are logic "0". In all other cases, the output is logic "0". The rectifier converts the alternating voltage (−0.4 to 0.4 V) in a single direction with half of the input voltage amplitude. In the case of the five-stage ring oscillator, the output signals vary between 0 and 0.8 V at a frequency of 9.7 Hz, which corresponds

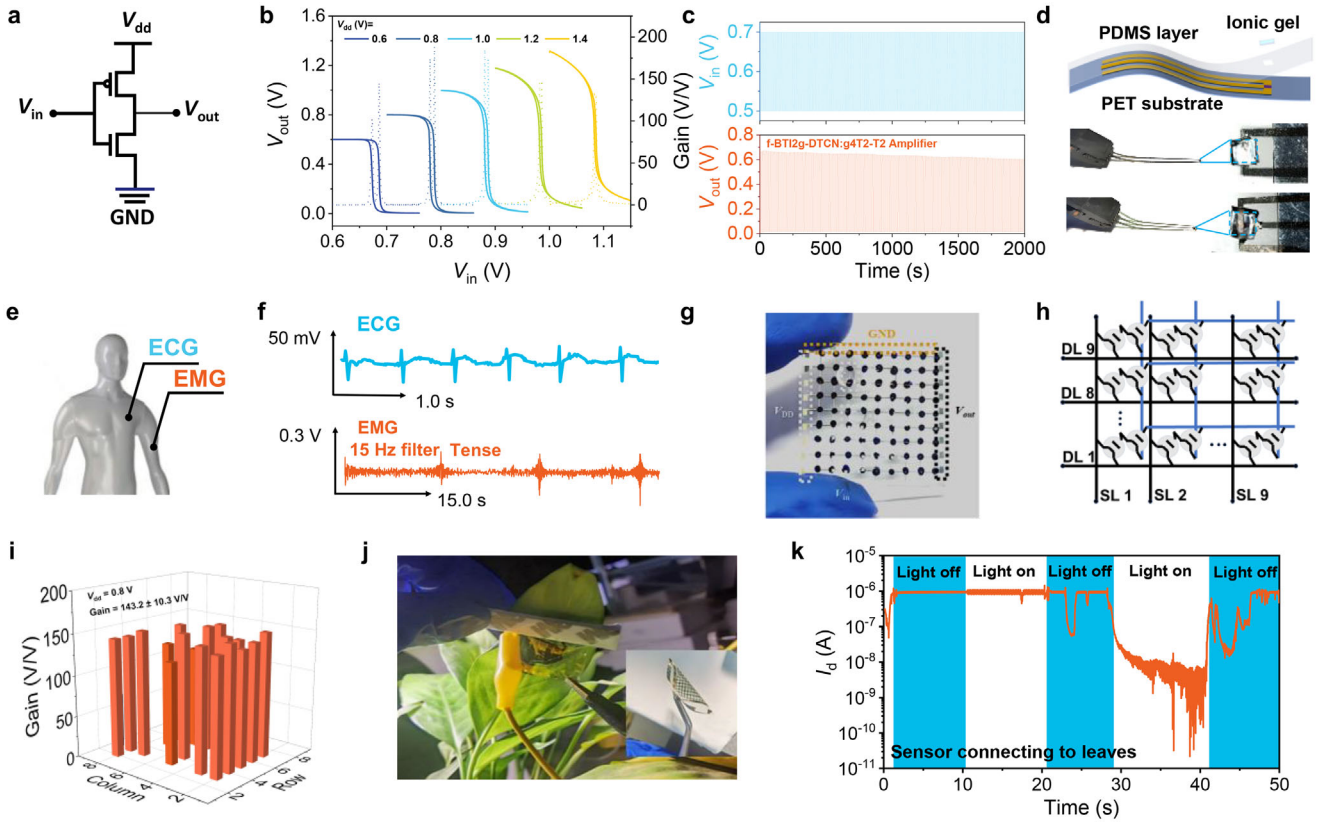

Figure 5. a) Illustration of a vertical inverter. b) Representative voltage output characteristic of a vertical inverter and voltage gain based on g4T2-T2 and PBTI2g-DTCN. c) Operational stability of the dynamic response of the vertical inverter based on g4T2-T2 and PBTI2g-DTCN. d) Schematic of the flexible sensors developed by cOECT and vOECT. e) Schematic illustration of in vitro recording for ECG and EMG. f) ECG and EMG signals monitored by amplified vOECT inverters. g) Optical images of inverter arrays comprising PBTI2g-DTCN and g4T2-T2 vOECTs. h) Circuit schematic of 9 × 9 vOECT active-matrix arrays based on vertical inverters. i) Voltage gain distribution of 22 randomly selected inverters in the 9 × 9 vertical traverse arrays gated by solid-state ion-gel and an Ag/AgCl electrode on vertical inverters. j) An optical picture shows a vOECT array that is attached to the back of a leaf. k) Recorded current as a function of time in the switching of illumination with an action potential (V_{ds} = 0.6 V) upon triggering the leaves.

to a propagation delay of 10.3 ms for each inverter stage. These logic circuits based on PBTI2g-DTCN and g4T2-T2 demonstrate their broad application potential in information processing.

3. Conclusion

To conclude, we have developed three BTI-based n-type OMIECs with distinctive imide group numbers in their backbones for OECT application. Compared to smaller-BTI-based PBTI1g-DTCN and larger-BTI3-based PBTI3g-DTCN, the mid-size BTI2-based PBTI2g-DTCN showed a high degree of backbone planarity, superior wettability, ordered packing, improved film crystallinity, and enhanced electron mobility. As a consequence, we achieved a remarkable $\mu_{e,OECT}$ of 0.84 $cm^2\ V^{-1}\ s^{-1}$, greatly larger than both of PBTI1g-DTCN and PBTI3g-DTCN. This results in the record $g_{m,norm}$ of 60.2 S cm^{-1} and μC^* of 287.8 F $cm^{-1}\ V^{-1}\ s^{-1}$ for PBTI2g-DTCN in n-type accumulation cOECTs and a remarkable $g_{m,A}$ of 71.8 µS $µm^{-2}$ in vOECTs with exceptional operation and storage stability. Interestingly, the vOECT exhibits dual-mode operation by component modulation, enabling both volatile and non-volatile states. This capability is leveraged to realize dynamic learning and memory functions, emulating CNN for image recognition and flexible biosensing, offering enhanced sensitivity for capturing electrocardiographic and electromyographic signals. This characteristic facilitates their incorporation into comprehensive biological signal monitoring systems.

Supporting Information

Supporting Information is available from the Wiley Online Library or from the author.

Acknowledgements

W.Y. and S.M. contributed equally to this work. The authors sincerely thank Jianhua Chen from the Department of Chemical Science and Technology, Yunnan University, for providing the Cin-Cell material. This work was supported by Shenzhen Science and Technology Innovation Commission (c818100617037 and JCYJ20230807093608017. This work was also supported by the Center for Computational Science and Engineering at the Southern University of Science and Technology (SUSTech). The authors acknowledge the assistance of SUSTech Core Research Facilities.

Conflict of Interest

The authors declare no conflict of interest.

Data Availability Statement

The data that support the findings of this study are available from the corresponding author upon reasonable request.

Keywords

bithiophene imide, high performance, organic bioelectronics, organic electrochemical transistors, organic mixed ionic-electronic conductors

Received: June 24, 2025
Revised: September 8, 2025
Published online:

[1] W. Huang, J. Chen, Y. Yao, D. Zheng, X. Ji, L.-W. Feng, D. Moore, N. R. Glavin, M. Xie, Y. Chen, R. M. Pankow, A. Surendran, Z. Wang, Y. Xia, L. Bai, J. Rivnay, J. Ping, X. Guo, Y. Cheng, T. J. Marks, A. Facchetti, *Nature* **2023**, *613*, 496.
[2] Y. Wang, S. Wustoni, J. Surgailis, Y. Zhong, A. Koklu, S. Inal, *Nat. Rev. Mater.* **2024**, *9*, 249.
[3] D. Khodagholy, T. Doublet, P. Quilichini, M. Gurfinkel, P. Leleux, A. Ghestem, E. Ismailova, T. Hervé, S. Sanaur, C. Bernard, G. G. Malliaras, *Nat. Commun.* **2013**, *4*, 1575.
[4] F. Hempel, J. K. Y. Law, T. C. Nguyen, R. Lanche, A. Susloparova, X. T. Vu, S. Ingebrandt, *Biosens. Bioelectron.* **2021**, *180*, 113101.
[5] R. Liu, X. Zhu, J. Duan, J. Chen, Z. Xie, C. Chen, X. Xie, Y. Zhang, W. Yue, *Angew. Chem., Int. Ed.* **2024**, *63*, 202315537.
[6] Y. van de Burgt, A. Melianas, S. T. Keene, G. Malliaras, A. Salleo, *Nat. Electron.* **2018**, *1*, 386.
[7] P. C. Harikesh, C.-Y. Yang, H.-Y. Wu, S. Zhang, M. J. Donahue, A. S. Caravaca, J.-D. Huang, P. S. Olofsson, M. Berggren, D. Tu, S. Fabiano, *Nat. Mater.* **2023**, *22*, 242.
[8] C.-Y. Yang, D. Tu, T.-P. Ruoko, J. Y. Gerasimov, H.-Y. Wu, P. C. Harikesh, M. Massetti, M.-A. Stoeckel, R. Kroon, C. Müller, M. Berggren, S. Fabiano, *Adv. Electron. Mater.* **2022**, *8*, 2100907.
[9] J. E. Tyrrell, K. Petkos, E. M. Drakakis, M. G. Boutelle, A. J. Campbell, *Adv. Funct. Mater.* **2021**, *31*, 2103385.
[10] R. B. Rashid, X. Ji, J. Rivnay, *Biosens. Bioelectron.* **2021**, *190*, 113461.
[11] J. J. Samuel, A. Garudapalli, A. A. Mohapatra, C. Gangadharappa, S. Patil, N. P. B. Aetukuri, *Adv. Funct. Mater.* **2021**, *31*, 2102903.
[12] J. Rivnay, S. Inal, A. Salleo, R. M. Owens, M. Berggren, G. G. Malliaras, *Nat. Rev. Mater.* **2018**, *3*, 17086.
[13] H. Liao, A. Savva, A. V. Marsh, Y.-Y. Yang, H. Faber, M. Rimmele, M. Sanviti, R. Zhou, A.-H. Emwas, J. Martín, T. D. Anthopoulos, M. Heeney, *Angew. Chem., Int. Ed.* **2024**, *63*, 202416288.
[14] I.-Y. Jo, D. Jeong, Y. Moon, D. Lee, S. Lee, J.-G. Choi, D. Nam, J. H. Kim, J. Cho, S. Cho, D.-Y. Kim, H. Ahn, B. J. Kim, M.-H. Yoon, *Adv. Mater.* **2024**, *36*, 2307402.
[15] R. K. Hallani, B. D. Paulsen, A. J. Petty II, R. Sheelamanthula, M. Moser, K. J. Thorley, W. Sohn, R. B. Rashid, A. Savva, S. Moro, J. P. Parker, O. Drury, M. Alsufyani, M. Neophytou, J. Kosco, S. Inal, G. Costantini, J. Rivnay, I. McCulloch, *J. Am. Chem. Soc.* **2021**, *143*, 11007.
[16] L. Bynens, K. Zhang, P. Cavassin, A. Goossens, J. Vanderspikken, T. C. H. Castillo, D. Tsokkou, A. Marks, A. Magni, K. Weaver, L. Lutsen, S. Inal, K. Vandewal, N. Banerji, W. Maes, *Adv. Funct. Mater.* **2025**, *35*, 2423913.
[17] H. Sun, J. Gerasimov, M. Berggren, S. Fabiano, *J. Mater. Chem. C* **2018**, *6*, 11778.
[18] Y. Lei, P. Li, Y. Zheng, T. Lei, *Mater. Chem. Front.* **2024**, *8*, 133.
[19] M. Ma, L. Zhang, M. Huang, Y. Kuang, H. Li, H. Yang, T. Yao, G. Ye, S. Shao, M.-H. Yoon, J. Liu, *Angew. Chem., Int. Ed.* **2025**, *64*, 202424820.
[20] Y. Kuang, T. Yao, S. Deng, J. Dong, G. Ye, L. Zhang, S. Shao, Z. Zhu, J. Liu, J. Liu, *Adv. Mater.* **2025**, *37*, 2417691.
[21] P. Li, J. Shi, Y. Lei, Z. Huang, T. Lei, *Nat. Commun.* **2022**, *13*, 5970.
[22] Z. S. Parr, J. Borges-González, R. B. Rashid, K. J. Thorley, D. Meli, B. D. Paulsen, J. Strzalka, J. Rivnay, C. B. Nielsen, *Adv. Mater.* **2022**, *34*, 2107829.
[23] K.-K. Liu, P. Li, Y. Lei, Z. Zhang, X. Pan, S. K. So, T. Lei, *Adv. Funct. Mater.* **2023**, *33*, 2300049.
[24] J. Shi, P. Li, X.-Y. Deng, J. Xu, Z. Huang, Y. Lei, Y. Wang, J.-Y. Wang, X. Gu, T. Lei, *Chem. Mater.* **2022**, *34*, 864.
[25] Z. Huang, P. Li, Y. Lei, X.-Y. Deng, Y.-N. Chen, S. Tian, X. Pan, X. Lei, C. Song, Y. Zheng, J.-Y. Wang, Z. Zhang, T. Lei, *Angew. Chem., Int. Ed.* **2024**, *63*, 202313260.
[26] A. Giovannitti, I. P. Maria, D. Hanifi, M. J. Donahue, D. Bryant, K. J. Barth, B. E. Makdah, A. Savva, D. Moia, M. Zetek, P. R. F. Barnes, O. G. Reid, S. Inal, G. Rumbles, G. G. Malliaras, J. Nelson, J. Rivnay, I. McCulloch, *Chem. Mater.* **2018**, *30*, 2945.
[27] D. Jeong, I.-Y. Jo, S. Lee, J. H. Kim, Y. Kim, D. Kim, J. R. Reynolds, M.-H. Yoon, B. J. Kim, *Adv. Funct. Mater.* **2022**, *32*, 2111950.
[28] D. Ohayon, A. Savva, W. Du, B. D. Paulsen, I. Uguz, R. S. Ashraf, J. Rivnay, I. McCulloch, S. Inal, *ACS Appl. Mater. Interfaces* **2021**, *13*, 4253.
[29] S. Cong, J. Chen, L. Wang, L. Lan, Y. Wang, H. Dai, H. Liao, Y. Zhou, Y. Yu, J. Duan, Z. Li, I. McCulloch, W. Yue, *Adv. Funct. Mater.* **2022**, *32*, 2201821.
[30] J. Chen, S. Cong, L. Wang, Y. Wang, L. Lan, C. Chen, Y. Zhou, Z. Li, I. McCulloch, W. Yue, *Mater. Horiz.* **2023**, *10*, 607.
[31] K. Feng, W. Shan, S. Ma, Z. Wu, J. Chen, H. Guo, B. Liu, J. Wang, B. Li, H. Y. Woo, S. Fabiano, W. Huang, X. Guo, *Angew. Chem., Int. Ed.* **2021**, *60*, 24198.
[32] J. Surgailis, A. Savva, V. Druet, B. D. Paulsen, R. Wu, A. Hamidi-Sakr, D. Ohayon, G. Nikiforidis, X. Chen, I. McCulloch, J. Rivnay, S. Inal, *Adv. Funct. Mater.* **2021**, *31*, 2010165.
[33] X. Chen, A. Marks, B. D. Paulsen, R. Wu, R. B. Rashid, H. Chen, M. Alsufyani, J. Rivnay, I. McCulloch, *Angew. Chem., Int. Ed.* **2021**, *60*, 9368.
[34] J. Guo, L. Q. Flagg, D. K. Tran, S. E. Chen, R. Li, N. B. Kolhe, R. Giridharagopal, S. A. Jenekhe, L. J. Richter, D. S. Ginger, *J. Am. Chem. Soc.* **2023**, *145*, 1866.
[35] A. Marks, X. Chen, R. Wu, R. B. Rashid, W. Jin, B. D. Paulsen, M. Moser, X. Ji, S. Griggs, D. Meli, X. Wu, H. Bristow, J. Strzalka, N. Gasparini, G. Costantini, S. Fabiano, J. Rivnay, I. McCulloch, *J. Am. Chem. Soc.* **2022**, *144*, 4642.
[36] H. Sun, M. Vagin, S. Wang, X. Crispin, R. Forchheimer, M. Berggren, S. Fabiano, *Adv. Mater.* **2018**, *30*, 1704916.
[37] J. Kim, R. M. Pankow, Y. Cho, I. D. Duplessis, F. Qin, D. Meli, R. Daso, D. Zheng, W. Huang, J. Rivnay, T. J. Marks, A. Facchetti, *Nat. Electron.* **2024**, *7*, 234.
[38] H.-Y. Wu, J.-D. Huang, S. Y. Jeong, T. Liu, Z. Wu, T. van der Pol, Q. Wang, M.-A. Stoeckel, Q. Li, M. Fahlman, D. Tu, H. Y. Woo, C.-Y. Yang, S. Fabiano, *Mater. Horiz.* **2023**, *10*, 4213.
[39] J. Chen, J. Yang, Y. Guo, Y. Liu, *Adv. Mater.* **2022**, *34*, 2104325.
[40] L. Shi, Y. Guo, W. Hu, Y. Liu, *Mater. Chem. Front.* **2017**, *1*, 2423.
[41] X. Guo, A. Facchetti, T. J. Marks, *Chem. Rev.* **2014**, *114*, 8943.
[42] Z. Chen, X. Ding, J. Wang, X. Guo, S. Shao, K. Feng, *Angew. Chem., Int. Ed.* **2025**, *64*, 202423013.
[43] K. Feng, H. Guo, H. Sun, X. Guo, *Acc. Chem. Res.* **2021**, *54*, 3804.
[44] Y. Wang, H. Guo, A. Harbuzaru, M. A. Uddin, I. Arrechea-Marcos, S. Ling, J. Yu, Y. Tang, H. Sun, J. T. López Navarrete, R. P. Ortiz, H. Y. Woo, X. Guo, *J. Am. Chem. Soc.* **2018**, *140*, 6095.
[45] X. Yan, M. Xiong, J.-T. Li, S. Zhang, Z. Ahmad, Y. Lu, Z.-Y. Wang, Z.-F. Yao, J.-Y. Wang, X. Gu, T. Lei, *J. Am. Chem. Soc.* **2019**, *141*, 20215.

[46] Y. Wang, H. Guo, S. Ling, I. Arrechea-Marcos, Y. Wang, J. T. López Navarrete, R. P. Ortiz, X. Guo, *Angew. Chem., Int. Ed.* **2017**, *56*, 9924.
[47] L. Ding, Z.-D. Yu, X.-Y. Wang, Z.-F. Yao, Y. Lu, C.-Y. Yang, J.-Y. Wang, J. Pei, *Chem. Rev.* **2023**, *123*, 7421.
[48] J. Rivnay, S. C. B. Mannsfeld, C. E. Miller, A. Salleo, M. F. Toney, *Chem. Rev.* **2012**, *112*, 5488.
[49] J. Veres, S. D. Ogier, S. W. Leeming, D. C. Cupertino, S. M. Khaffaf, *Adv. Funct. Mater.* **2003**, *13*, 199.
[50] M. Abarkan, A. Pirog, D. Mafilaza, G. Pathak, G. N'Kaoua, E. Puginier, R. O'Connor, M. Raoux, M. J. Donahue, S. Renaud, J. Lang, *Adv. Sci.* **2022**, *9*, 2105211.
[51] P. Li, W. Sun, J. Li, J.-P. Chen, X. Wang, Z. Mei, G. Jin, Y. Lei, R. Xin, M. Yang, J. Xu, X. Pan, C. Song, X.-Y. Deng, X. Lei, K. Liu, X. Wang, Y. Zheng, J. Zhu, S. Lv, Z. Zhang, X. Dai, T. Lei, *Science* **2024**, *384*, 557.
[52] K. Feng, W. Shan, J. Wang, J.-W. Lee, W. Yang, W. Wu, Y. Wang, B. J. Kim, X. Guo, H. Guo, *Adv. Mater.* **2022**, *34*, 2201340.
[53] K. Ding, J. Wang, Y. Zhou, H. Tian, L. Lu, R. Mazzarello, C. Jia, W. Zhang, F. Rao, E. Ma, *Science* **2019**, *366*, 210.
[54] H. Shim, F. Ershad, S. Patel, Y. Zhang, B. Wang, Z. Chen, T. J. Marks, A. Facchetti, C. Yu, *Nat. Electron.* **2022**, *5*, 660.
[55] D. Liu, Q. Shi, S. Dai, J. Huang, *Small* **2020**, *16*, 1907472.
[56] Z. Xie, C. Zhuge, Y. Zhao, W. Xiao, Y. Fu, D. Yang, S. Zhang, Y. Li, Q. Wang, Y. Wang, W. Yue, I. McCulloch, D. He, *Adv. Funct. Mater.* **2022**, *32*, 2107314.
[57] S. Cong, J. Chen, M. Xie, Z. Deng, C. Chen, R. Liu, J. Duan, X. Zhu, Z. Li, Y. Cheng, W. Huang, I. McCulloch, W. Yue, *Sci. Adv.* **2025**, *10*, adq9405.
[58] Y. Yin, S. Wang, R. Weng, N. Xiao, J. Deng, Q. Wang, Z. Wang, P. K. L. Chan, *Small Sci.* **2024**, *4*, 2400415.
[59] S. Wang, X. Chen, C. Zhao, Y. Kong, B. Lin, Y. Wu, Z. Bi, Z. Xuan, T. Li, Y. Li, W. Zhang, E. Ma, Z. Wang, W. Ma, *Nat. Electron.* **2023**, *6*, 281.
[60] W. Li, N. Matsuhisa, Z. Liu, M. Wang, Y. Luo, P. Cai, G. Chen, F. Zhang, C. Li, Z. Liu, Z. Lv, W. Zhang, X. Chen, *Nat. Electron.* **2021**, *4*, 134.